Eur. Phys. J. Plus (2023) 138:1124
https://doi.org/10.1140/epjp/s13360-023-04744-1

THE EUROPEAN PHYSICAL JOURNAL PLUS

Regular Article

Stability analysis of exciton, charged excitons, and biexciton in an InP/GaAs/GaSb type-II quantum dot heteronanostructure: a comparison of binding energy and diamagnetic susceptibility

Fatih Koç[a]

Department of Metallurgical and Materials Engineering, Ahi Evran University, Kırşehir, Turkey

Received: 5 August 2023 / Accepted: 24 November 2023

Abstract The present study focused on investigating the total energies, binding energies, and diamagnetic susceptibilities of excitons, negative and positive trions, and biexcitons within an InP/GaAs/GaSb type-II quantum dot heteronanostructure. The analysis has been carried out by varying the InP core radius, GaAs and GaSb layer thicknesses, and temperature. To obtain the energy levels and wavefunctions of the system, the Poisson–Schrödinger equation has been solved under the effective mass approximation and BenDaniel–Duke boundary conditions, considering the dielectric mismatch. The results of the calculations have revealed that while diamagnetic susceptibility could provide reliable information about the stability of the exciton, it has not offered the same level of accuracy when assessing the stability of the negative and positive trion and biexciton. Additionally, it has been observed that the dielectric mismatch effect can be influential, to the extent of reversing the expected trend in the binding energy, particularly when the GaAs layer thickness varies. On the other hand, the effect of temperature has been found to be limited and negligible due to the strong confinement of the quantum dot heteronanostructure.

1 Introduction

Semiconductor quantum dot heteronanostructures (QD-HNSs) confine various quasi-particles, such as excitons [composed of an electron (e) and a hole (h)], negative trions (2e-1h) and positive trions (1e-2h), also known as charged excitons, and biexcitons (2e-2h), through optical excitation. The confinement is achieved by the potential of the structure in all three spatial dimensions. These confined quasi-particles in QD-HNSs exhibit unique responses to factors like changes in size, geometry, electric field, magnetic field, electromagnetic waves, pressure, and temperature. As a result, these structures are currently being utilized or considered as potential candidates in a wide range of applications, including quantum sensors, quantum dot solar cells, medicine, quantum information, and quantum computation.

QD-HNSs offer unique advantages in various application areas based on the type of quasi-particle they confine. Excitons (X) and biexcitons (XX), neutral-charged quasi-particles, play a crucial role in the fields of quantum information and quantum computation. In QD-HNSs with strong quantum confinement, excitons emerge with energy levels akin to atomic states, representing a simple two-level quantum system. These excitons can be treated as single qubits, and their coherent control is achievable through optical Rabi oscillation [1–3]. Conversely, biexcitons form a more complex four-level quantum system, allowing for the construction of coherent combinations of quantum states. The four distinguishable states of a biexciton can generate entangled photon pairs, enabling fundamental quantum operations involving two qubits through radiative recombination [4–7]. The application areas of exciton and biexciton structures extend beyond quantum information and quantum computation. They hold promise in various fields, including photovoltaic devices [8], light-emitting diodes (LEDs) [9, 10], lasers [11–13]and more [12, 14].

On the other hand, negative (X^-) and positive (X^+) trions, initially proposed by Lampert [15], are quasi-particles with positive or negative charges, distinguishing them from excitons and biexcitons. Trions, with their excess charge in the structure, display unique responses to manipulation tools such as electric fields, magnetic fields, and changes in size, setting them apart from their neutral counterparts. At the same time, this additional charge enables them to showcase charge-tunable electronic and optical properties, enhancing their versatility for various applications [16–18]. Additionally, trions offer the capability of optically manipulating the spin of QD-HNSs through their circularly polarized emissions. Thanks to these properties, trions are predicted to find applications in the field of quantum communication and spin-based qubits [19]. Furthermore, recent studies have focused more on investigating trions in 2D materials, resulting in promising developments in the field of trion-based optoelectronic devices [20–23].

[a] e-mail: fatih.koc@msn.com (corresponding author)

Published online: 18 December 2023

As evident, the application areas and usage patterns of QD-HNSs are directly influenced by the quasi-particles trapped within the structure, but their versatility extends beyond this factor. The bound or unbound state [24] of the quasi-particles in QD-HNSs contributes to the advantages of these structures in diverse application areas. As is well-known, in the bound state of X, X^-, X^+, and XX, all charges within the structure behave collectively as a single particle influenced by the attractive Coulomb potential. In contrast, in the unbound state of X, the Coulomb potential between the electron and the hole becomes negligible, and they exist as independent free particles within the structure. Similarly, in X^-, an X and an electron move apart from each other, in X^+, an X and a hole move independently, and in XX, two X move independently of each other. These distinctions between the bound and unbound states of quasi-particles give rise to diverse options in the application areas and control mechanisms of QD-HNS [24]. For example, the emission of the bound excitons can be utilized as laser media, whereas the unbound excitons find applications in photovoltaics [25]. Considering these factors, including their widespread use, potential applications, sensitivity to internal and external parameters, and effective response to various tuning tools, QD-HNSs continue to be subjects of intensive study and research.

This study aimed to conduct a comprehensive numerical analysis of the total energy, binding energy, and diamagnetic susceptibility of X, X^-, X^+, and XX quasi-particles within a spherical symmetric InP/GaAs/GaSb type-II (electron(s) and hole(s) localize to different spatial regions) QD-HNS [26]. In this structure, the electron(s) are localized within the InP core, while the hole(s) are confined to the GaSb shell. Additionally, GaAs is employed as an advanced tool for wave function engineering to enhance the clarity of the effects of the distance between electron(s) and hole(s) on the investigated parameters.

The total energy analysis contributes to the determination of absorption frequencies, whereas the binding energy provides valuable insights into whether the quasi-particles within the quantum dot structure are bound or unbound. Moreover, the diamagnetic susceptibility parameter holds significance in experimental studies as it can be measured and provides information about the stability of excitonic formations [27–30].

To investigate these aspects, the Poisson–Schrödinger equation has been solved using the effective mass approximation, and BenDaniel–Duke boundary conditions have been implemented, taking into account the dielectric mismatch. The study considered varying sizes of the structure and temperature as variables to analyze their influences on the investigated parameters.

2 Model and theory

Here, a spherically symmetric InP/GaAs/GaSb type-II QD-HNS has been considered. Schematic representation and potential profile of the structure are given in Fig. 1.

In the case of excitonic states, the energy levels and their corresponding wave functions can be obtained by the self-consistent solution of the Schrödinger-Poisson equation. A detailed explanation of this calculation method has been provided in our previous studies [31, 32]. In the effective mass approximation and BenDaniel–Duke boundary conditions [33], the single-particle Schrödinger equations of electron and hole are given separately using the Hartree approximation as [34]:

$$\left[-\frac{\hbar^2}{2}\nabla_r\left(\frac{1}{m_e^*(r,T)}\nabla_r\right)+V_e(r,T)-q_e\Phi_h+q_e\Phi_e+V_{xc}^{e-e}[\rho_e(r,T)]\right]R_e(r,T)=\varepsilon_e(T)R_e(r,T), \tag{1}$$

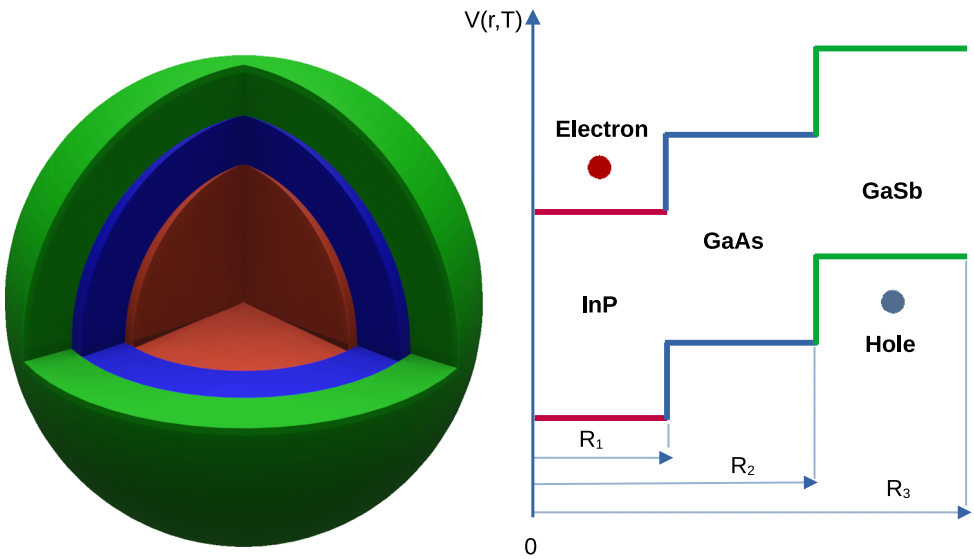

Fig. 1 Representation of InP/GaAs/GaSb QD-HNS and its potential profile. While the electron is confined into the InP core, the hole localizes to GaSb shell

and

$$\left[-\frac{\hbar^2}{2}\nabla_r\left(\frac{1}{m_h^*(r,T)}\nabla_r\right)+V_h(r,T)-q_h\Phi_e+q_h\Phi_h+V_{xc}^{h-h}[\rho_h(r,T)]\right]R_h(r,T)=\varepsilon_h(T)R_h(r,T). \tag{2}$$

Here, e and h are symbolize the electron and hole, respectively, $\hbar$ is the reduced Planck constant, q_e and q_h are charge of the particles. The first terms of the equations are the kinetic energy terms of the electron and hole, and $m_{e,h}^*(r,\ T)$ refer to radial and temperature-dependent effective mass of the charges. The second terms of the equations, $V_e(r,\ T)$ and $V_h(r,\ T)$, correspond to the temperature-dependent band alignment-induced confinement potentials of the particles. The third and fourth terms represent attractive and repulsive electrostatic Coulomb potentials of the particles, respectively. The remaining terms, V_{xc}^{e-e} and V_{xc}^{h-h}, are the exchange–correlation potentials between the same charges, $R_e(r,\ T)$ and $R_h(r,\ T)$ are the radial wave functions and $\varepsilon_e(T)$ and $\varepsilon_h(T)$ are the energy eigenvalues. When the equations are examined, it is seen that these two equations become a coupled equations owing to the attractive Coulomb term between the electron(s) and the hole(s). In this study, the exchange–correlation potential between the electron and hole has been neglected to simplify calculations, since it contributes relatively little.

The temperature and position-dependent effective mass of the electron and hole are given as [35]

$$m_e^*(r,T)=m_0\left[1+\frac{E_P}{3}\left(\frac{2}{E_g(T)}+\frac{1}{E_g(T)+\Delta_0}\right)\right]^{-1} \tag{3}$$

and

$$m_h^*(r,T)=m_h(r,0)\left(\frac{E_g(T)}{E_g(0)}\right) \tag{4}$$

where m_0 is the free electron mass, E_P is the Kane energy, Δ_0 is the spin-orbit splitting energy and $E_g(0)$ and $m_h(r,\ 0)$ are the gap energy and effective mass of the hole at $T=0$ K, respectively. The temperature-dependent gap energy $E_g(T)$ is [35]

$$E_g(T)=E_g(0)-\frac{\alpha T^2}{(T+\beta)}. \tag{5}$$

Here, α and β are the Varshni parameters of the materials [35].

2.1 Exciton

As is well known, the exciton is a quasi-particle formed by the bonding of electron and hole pairs to each other thanks to the Coulomb potential. In the case of the single exciton, while obtaining the energy levels and wave functions the repulsive Coulomb and the exchange–correlation potential terms are neglected in Eqs. (1) and (2) because there is only one electron and one hole. In the first step, attractive Coulomb terms are taken as zero in the equations and non-interacting single particle energy levels and corresponding wave functions are obtained. In the second step, the electrostatic Coulomb potentials are calculated by substituting these wave functions into following Poisson equations [34],

$$\vec{\nabla}\kappa(r)\vec{\nabla}\Phi_e=q_e\rho_e(r,T),\qquad \vec{\nabla}\kappa(r)\vec{\nabla}\Phi_h=-q_h\rho_h(r,T), \tag{6}$$

where $\kappa(r,\ T)$ is the temperature-dependent dielectric constant of the material, $\rho_{e(h)}$ is the density of the electron(hole) [36]. In the third step, Eqs. (1) and (2) are re-solved by submitting these potentials and new energy levels and wave functions have been obtained including the attractive Coulomb effect. Finally, the last two steps are repeated until the desired convergence is achieved and the final energy levels and corresponding wave functions are obtained. The total energy, binding energy and diamagnetic susceptibility of the exciton have been calculated from final energies and wave functions of the electron and hole.

The total energy of the exciton strongly depends on the dimensions of the QD-HNSs, determines the absorption frequency and contains information about the optical interaction. For this reason, the examination of the total energy of the exciton is important in terms of giving an idea about the QD-HNSs. For an exciton, the total energy is given as [36],

$$E_X^{tot}(T)=E_g(T)+\varepsilon_e(T)+\varepsilon_h(T)-\varepsilon_{e-h}(T) \tag{7}$$

here, $\varepsilon_{e-h}(T)$ is the temperature-dependent attractive Coulomb energy between the electron and hole. Since the term $\varepsilon_{e-h}(T)$ is included in both Eqs. (1) and (2), its effect is calculated twice and one of them must be deducted [36].

The bound or unbound regime of the exciton plays a key role in device applications and has a direct effect on optical properties. In this context, calculation and measurement of the exciton binding energy are especially important for device applications. For a single exciton, there is only the attractive Coulomb effect between the electron and the hole, and this effect directly determines the binding energy. The binding energy of the single exciton calculated by means of [36]

$$E_X^B(T)=E_g(T)+\varepsilon_e^0(T)+\varepsilon_h^0(T)-E_X^{tot}(T), \tag{8}$$

here, $\varepsilon_e^0(T)$ and $\varepsilon_h^0(T)$ are the temperature-dependent non-interacting single particle electron and hole energies.

Diamagnetic susceptibility is another important parameter that can be measured experimentally and provides valuable insights into the stability of excitonic formations. This parameter can be given as [30, 37]

$$\chi_{dia}^{X}(T) = -\frac{e^2}{6\mu_X^*(T)\kappa(r,T)c^2}\langle r_X^2\rangle, \tag{9}$$

where c is the velocity of light, $\mu_X^*(T)$ is the reduced mass of the exciton. $\langle r^2\rangle$ is the expectation value of the exciton radius squared [38–40] and it can be calculated from

$$\langle r_X^2\rangle = \langle\psi_X|r^2|\psi_X\rangle. \tag{10}$$

Here, the radial exciton wavefunction $\psi_X = N\psi_e\psi_h$, where N is the normalization constant, ψ_e and ψ_h refer to radial wavefunctions of the electron and hole, respectively, obtained from Eqs. (1) and (2).

2.2 Trions

Trions, also known as charged excitons, are quasi-particles composed of three charges. Formations consisting of two electrons(holes) and one hole(electron) called negative(positive) trion. In the trionic state calculations, the steps in the excitonic state are repeated with small differences. For the negative trion, since there are two electrons, in addition to attractive Coulomb potential term, the repulsive Coulomb and exchange–correlation potential terms are included in Eq. (1) but not in Eq. (2). For the positive trion, these potential terms are included in Eq. (2), while Eq. (1) does not include these potentials. After these arrangements, single particle energy levels and corresponding wave functions are obtained by the self-consistent calculations following the steps in the excitonic state.

The total energy of the negative and positive trion can be written as,

$$\begin{aligned} E_{X^-}^{tot}(T) = {} & E_g(T) + 2\varepsilon_e(T) + \varepsilon_h(T) - \varepsilon_{e-h}^{X^-}(T) - \frac{q_e}{2}\int \phi_e\rho_e(r,T)d^3r \\ & + E_{xc}^{e-e}[\rho_e(r,T)] - \int \rho_e(r,T)V_{xc}^{e-e}d^3r, \end{aligned} \tag{11}$$

and

$$\begin{aligned} E_{X^+}^{tot}(T) = {} & E_g(T) + \varepsilon_e(T) + 2\varepsilon_h(T) - \varepsilon_{e-h}^{X^+}(T) - \frac{q_h}{2}\int \phi_h\rho_h(r,T)d^3r \\ & + E_{xc}^{h-h}[\rho_h(r,T)] - \int \rho_h(r,T)V_{xc}^{h-h}d^3r, \end{aligned} \tag{12}$$

where $E_{xc}^{e-e}[\rho_e(r,\ T)]$ and $E_{xc}^{h-h}[\rho_h(r,\ T)]$ are the density-dependent exchange–correlation energies of the electrons and holes, V_{xc}^{e-e} and V_{xc}^{h-h} are the exchange–correlation potentials of the electrons and holes, respectively [41]. These terms are discussed in detail in our previous work [32].

The binding energies of the negative and positive trions are defined as

$$\begin{aligned} E_B^{X^-}(T) &= E_X^{tot}(T) + \varepsilon_e^0(T) - E_{X^-}^{tot}(T), \\ E_B^{X^+}(T) &= E_X^{tot}(T) + \varepsilon_h^0(T) - E_{X^+}^{tot}(T). \end{aligned} \tag{13}$$

The diamagnetic susceptibility of the negative and positive trions is determined by means of

$$\begin{aligned} \chi_{dia}^{X^-}(T) &= -\frac{e^2}{6\mu_{X^-}^*(T)\kappa(r,T)c^2}\langle r_{X^-}^2\rangle, \\ \chi_{dia}^{X^+}(T) &= -\frac{e^2}{6\mu_{X^+}^*(T)\kappa(r,T)c^2}\langle r_{X^+}^2\rangle. \end{aligned} \tag{14}$$

Here, $\mu_{X^-}^*$ and $\mu_{X^+}^*$ are the reduced mass of the negative and positive trion, respectively. $\langle r_{X^-}^2\rangle$ denotes expectation value of the negative trion radius squared and $\langle r_{X^+}^2\rangle$ refer to expectation value of the positive trion radius squared.

2.3 Biexciton

A biexciton consists of two electrons and two holes, and this system stands out as simple four-level system in quantum information and quantum computation based on to construct coherent combinations of quantum states. In the biexcitonic state calculations, all effects, attractive Coulomb, repulsive Coulomb and exchange correlation potentials, are included in both Eq. (1) and (2) and these two equations are solved in a self-consistent manner and single particle energies and wave functions are obtained.

The total energy of a biexciton is calculated from

$$E_{XX}^{tot}(T) = 2E_g(T) + E_e^{tot}(T) + E_h^{tot}(T) - \varepsilon_{e-h}(T) - \frac{q_e}{2}\int \phi_e \rho_e(r,T) d^3r - \frac{q_h}{2}\int \phi_h \rho_h(r,T) d^3r + E_{xc}^{e-e}[\rho_e(r,T)] - \int \rho_e(r,T) V_{xc}^{e-e} d^3r + E_{xc}^{h-h}[\rho_h(r,T)] - \int \rho_h(r,T) V_{xc}^{h-h} d^3r. \quad (15)$$

The binding energy of the biexciton can be calculated by means of [42],

$$E_B(XX) = 2E_X^{tot}(T) - E_{XX}^{tot}(T). \quad (16)$$

The diamagnetic susceptibility of the biexciton can be calculated from

$$\chi_{dia}^{XX}(T) = -\frac{e^2}{6\mu_{XX}^*(T)\kappa(r,T)c^2}\langle r_{XX}^2 \rangle \quad (17)$$

where μ_{XX}^* is the reduced mass of the biexciton and $\langle r_{XX}^2 \rangle$ corresponds to expectation value of the biexciton radius squared.

3 Results and discussion

This study has been focused on analyzing the total energy, binding energy, and diamagnetic susceptibility of X, X^-, X^+, and XX quasi-particles in an InP/GaAs/GaSb type-II QD-HNS embedded in a glass matrix. The analysis was conducted by taking into account the dimensions of InP, GaAs, and GaSb, as well as the temperature. By default, the InP core radius, GaAs, and GaSb layer thicknesses were set to 0.8 a_0, and the temperature was set to 0 K. The overall size of the QD-HNS has been kept constant at 6.0 a_0, which includes the glass matrix. The calculations have been performed using atomic units, where $\hbar = m_0 = e = 1$ and $c = 137$. The effective exciton Bohr radius, a_0, and the effective Rydberg energy have been determined based on InP parameters, yielding values of 71.7 Å and 10.46 meV, respectively. The material parameters utilized in the calculations are presented in Table 1. Furthermore, dielectric mismatch has also been taken into account due to its significant impact in the calculations.

In the depicted InP/GaAs/GaSb type-II QD-HNS shown in Fig. 1, the electrons are confined within the InP core, and the holes localize to the GaSb shell. However, as shown in Fig. 2 in small core-sized QD-HNS, electrons may diffuse throughout the structure, leading to quasi-type-I behavior. The independent adjustment of the electron and hole energies based on the layer size in InP/GaAs/GaSb type-II QD-HNS enables a clearer observation of their individual effects on the investigated parameters. Moreover, in this model structure, as can be clearly seen from Fig. 2 (middle row) varying the size of the GaAs interlayer allows for a more focused examination of the influence of charge separation on binding energy and diamagnetic susceptibility while minimizing the impact on electron and hole energies.

Figure 3a illustrates the variations in total energies of the X, X^-, X^+, and XX as a function of the InP core radius. As anticipated, the total energies of all four quasi-particles demonstrate an initial rapid decline as the core radius increases, followed by a more stable trend. The electron energy decreases rapidly with the expansion of the core, eventually reaching a lower energy compared to the hole. While the thickness of the GaSb layer, where the hole is confined, remains constant (there is no change in hole energy), the hole energy becomes increasingly dominant in the total energy as the core radius increases. Consequently, the total energies exhibit less variation with the expanding core radius after a certain core radius.

Figure 3b illustrates the impact of the core radius on the binding energy. A positive binding energy represents a bound state where the attractive Coulomb effect dominates. Conversely, a negative binding energy indicates an unbound state where the repulsive Coulomb effect prevails. As anticipated, the binding energy of X remains positive across all core radii and shows a decreasing trend as the core radius increases. The other quasi-particles demonstrate a more intricate variation in binding energy as the core radius increases. The binding energies of X^- and XX are positive for core radii up to 0.5 a_0, but become negative for larger core radii. Up to 0.5 a_0, the wave function of the electrons spreads throughout the entire structure, leading to a quasi-type-I localization regime. In this regime, the electron and hole are in close proximity, resulting in a dominant attractive Coulomb potential. Once this core radius is exceeded, the electrons become localized within the core, causing a transition to the type-II regime. In the type-II

Table 1 The material parameters used in the calculations

	$m_h^*(0)$	$\kappa(0)$	$E_g(0)$ (eV)	E_P (eV)	α (meV/K)	β (K)	Δ_0 (meV)	$d\kappa/dT$ (10^{-3}K^{-1})
InP	0.69 [35]	12.90 [35]	1.422 [35]	17.0 [43]	0.45 [35]	335 [35]	114 [35]	2.66 [35]
GaAs	0.55 [35]	12.90 [35]	1.517 [35]	27.0 [43]	0.55 [35]	225 [35]	341 [35]	1.58 [35]
GaSb	0.37 [35]	15.50 [35]	0.809 [35]	27.0 [43]	0.53 [35]	234 [35]	780 [35]	

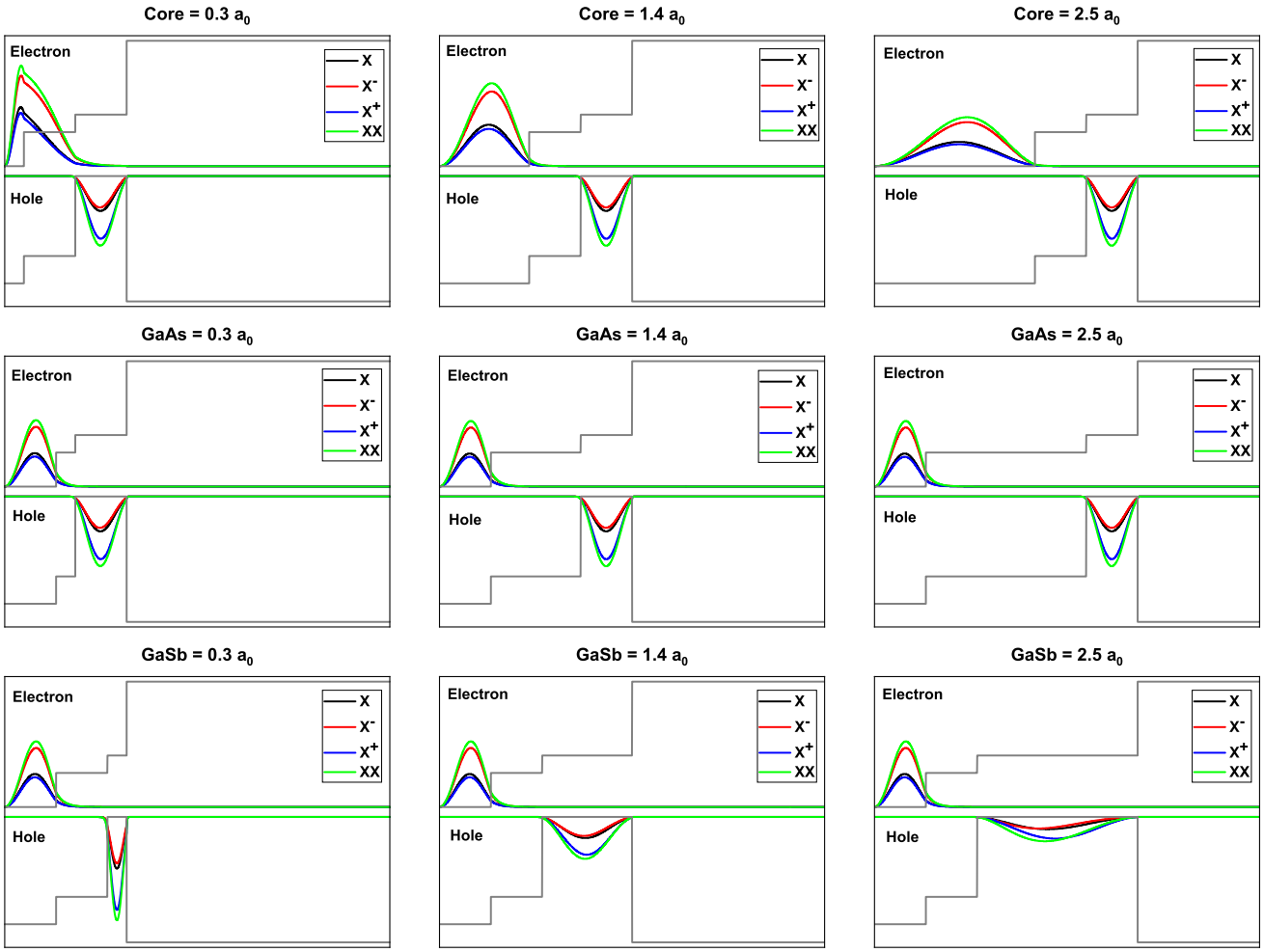

Fig. 2 Density plots showing the spatial distribution of electrons and holes in QD-HNS for various core, GaAs, and GaSb sizes. Unspecified dimensions are set to 0.8 a_0, with the total QD-HNS size fixed at 6.0 a_0

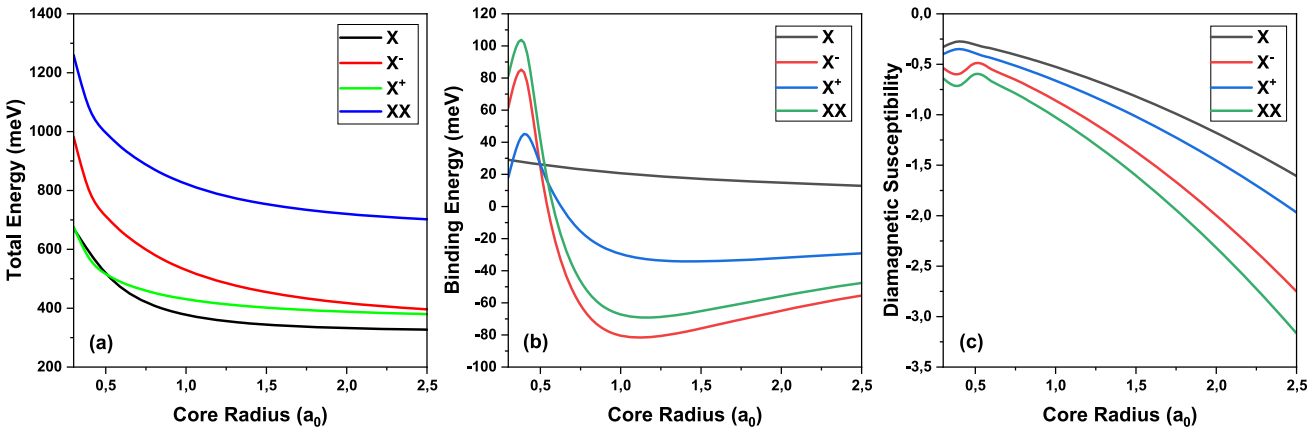

Fig. 3 Total energies (left), binding energies (middle) and diamagnetic susceptibilities (right) of the X, X^-, X^+, and XX as a function of the core radius

regime, the electrons and holes are farther apart, causing a weaker attractive Coulomb effect and resulting in a negative binding energy. However, for X^+, the quasi-type-I regime persists until the core radius reaches 0.6 a_0, owing to the strong attractive Coulomb potential generated by the presence of the two holes acting on the electron. Another notable point to mention is that, for core radii larger than 1.0 a_0, the binding energy of X^- and XX increases, while the binding energy of X^+ remains relatively constant. This behavior can be attributed to the repulsive Coulomb potential between the two electrons in X^- and XX, which decreases as the

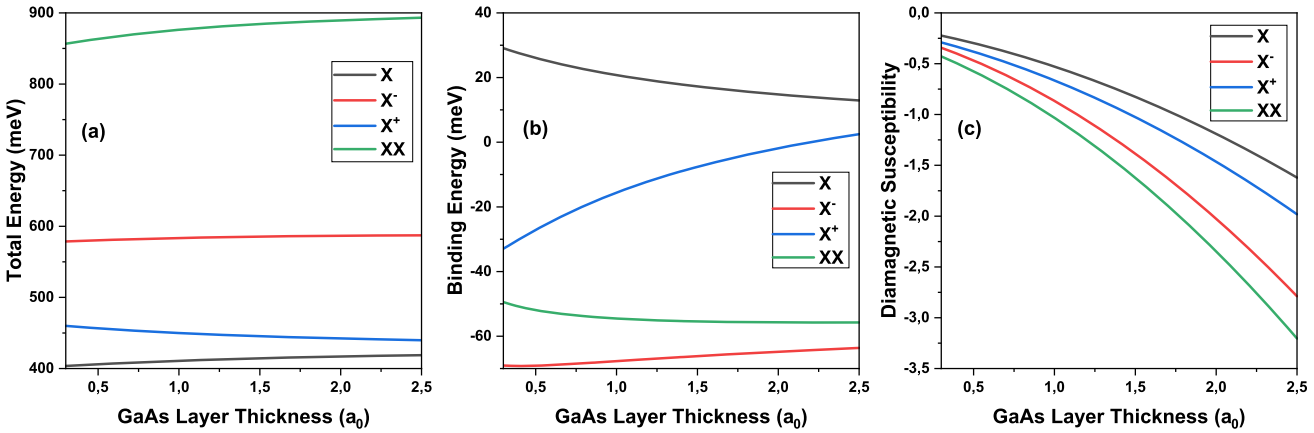

Fig. 4 Total energies (left), binding energies (middle) and diamagnetic susceptibilities (right) of the X, X^-, X^+, and XX as a function of the GaAs interlayer thickness

core radius increases due to the confinement of the electrons in a larger volume. On the other hand, the thickness of the GaSb layer, where the holes are localized, remains constant, leading to an unchanged repulsive Coulomb potential between the holes. As the core radius increases the attractive Coulomb potential weakens, and the repulsive Coulomb potential between the holes becomes the primary factor determining the binding energy of X^+.

Figure 3c illustrates the effect of core radius variation on the diamagnetic susceptibility of X, X^-, X^+, and XX. It can be observed that the diamagnetic susceptibility of all quasi-particles increases with the increase in core radius. This is an expected result since the diamagnetic susceptibility is directly influenced by the distance between electrons and holes. Analyzing the electron and hole densities in Fig. 2 (first row), it is clear that the spatial separation between the electron and the hole increases with increasing core radius. This phenomenon occurs because the electron is pulled toward the core. Consequently, this increase in spatial separation contributes to a higher diamagnetic susceptibility, which serves as a measure of the spatial distance between the electron and the hole. Moreover, for the bound states, there is a distinct fluctuation in the diamagnetic susceptibility that deviates from the overall trend observed at higher core radii. This fluctuation is attributed to the changing reduced masses, as the electron density disperses throughout the QD-HNS at smaller core radii, relaxes as the core radius increases, and gradually retracts toward the core region. On the other hand, for unbound states, a monotonic trend is observed as the core radius increases, displaying a smoother and more consistent behavior. Another notable finding is the similarity between the trend and values of diamagnetic susceptibility of X^+ and X. Similarly, the diamagnetic susceptibility of X^- bears considerable resemblance, both in trend and values, to that of XX.

Figure 4a illustrates the impact of GaAs interlayer thickness variation on the total energies of X, X^-, X^+, and XX. Due to the localization of electrons in the InP core and the presence of holes in the GaSb outer layer, changes in the GaAs interlayer thickness have minimal effect on the kinetic energies of both electrons and holes. However, as shown in the figure, slight changes are observed in the total energies of all four quasi-particles. These changes can be explained by the presence of image charges arising from the dielectric mismatch. Since InP and GaAs have the same dielectric constant, no image charges are induced in the GaAs interlayer for the electrons localized in the InP core. However, the higher dielectric constant of GaSb compared to GaAs leads to the induction of image charges in the GaAs interlayer with the same charge as the holes, resulting in a repulsive Coulomb potential between the holes and these image charges [44]. In other words, the induced image charges in GaAs generate a repulsive potential for the holes that opposes the attractive Coulomb potential of the electrons. In this context, the increase in the total energy of X with the increasing GaAs layer thickness can be directly attributed to the decrease in the strength of the attractive Coulomb interaction between the electron and hole. Similarly, the total energies of X^- and XX also increase with increasing GaAs interlayer thickness, indicating a stronger repulsive Coulomb effect between the same charges and a reduced attractive Coulomb effect. However, X^+ stands out from the other quasi-particles as it demonstrates a decreasing trend in total energy. With an increase in the GaAs layer thickness, the distance between the holes and their induced image charges also increases, leading to a reduction in the repulsive Coulomb effect. As a result, the total energy of X^+ decreases due to the growing influence of the attractive Coulomb potential. On the other hand, the absence of a similar trend in XX can be attributed to the compensating repulsive Coulomb effect between the two electrons, which counteracts the loss of holes.

Figure 4b demonstrates the relationship between the binding energies of the X, X^-, X^+, and XX and the GaAs layer thickness. The binding energy of X is positive for all of the GaAs layer thicknesses, and it follows the expected decreasing trend as the distance between the electron and hole increases with the GaAs thickness. In contrast, the binding energy of X^- remains negative for all GaAs thicknesses, but it increases as the GaAs layer becomes thicker. This can be attributed to the dominance of the attractive Coulomb potential between the electrons and the hole, which outweighs the repulsive interaction between the hole and its induced image charge in the GaAs layer. As the GaAs layer thickness increases, the repulsive interaction between the hole and its image charge weakens, allowing the attractive Coulomb potential to play a more significant role. Similar behavior is observed for X^+.

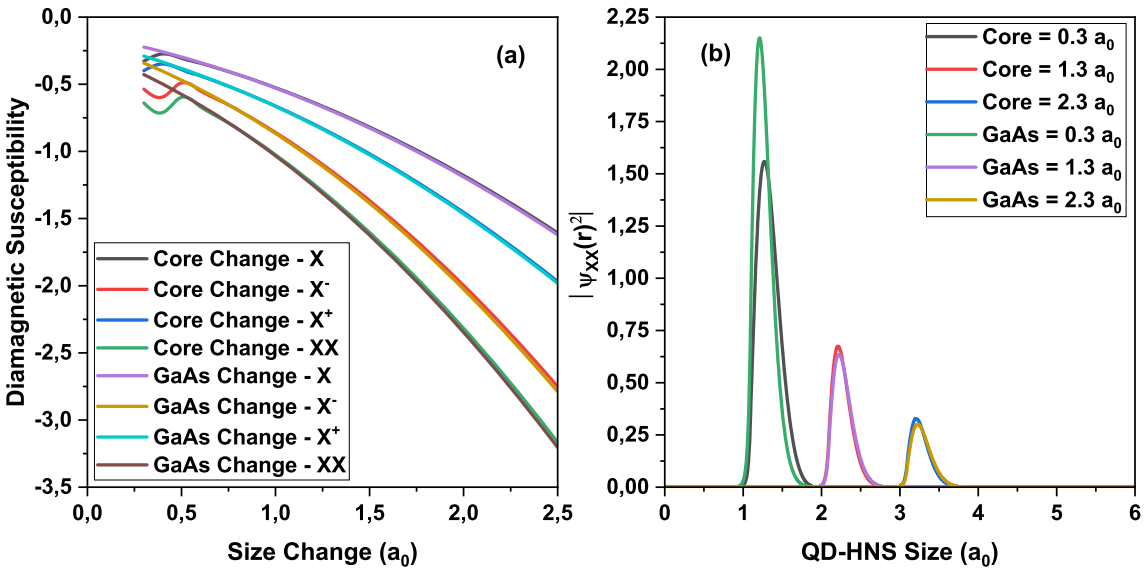

Fig. 5 **a** Depicts the variation of diamagnetic susceptibility with core radius/GaAs layer thickness. Here, while the core radius (GaAs layer thickness) is variable, the GaAs layer thickness (core radius) is fixed at 0.8 a_0. **b** provides the biexciton probability densities for different core radius and GaAs layer thickness. For core radius values of 0.3, 1.3, and 2.3 a_0, the GaAs layer thickness is fixed at 0.8 a_0. Conversely, for GaAs layer thickness values of 0.3, 1.3, and 2.3 a_0, the core radius is fixed at 0.8 a_0

The binding energy of X^+ increases with the GaAs layer thickness, following a similar trend as X^-. However, the increase is more pronounced for X^+ due to the stronger attractive Coulomb potential exerted by the holes and their induced image charges on the electron. After the GaAs layer thickness exceeds 2.1 a_0, X^+ forms a bound state, characterized by a positive binding energy. On the other hand, the binding energy of XX shows a decreasing trend as the GaAs layer thickness increases, similar to X. This decrease can be explained by the diminishing attractive Coulomb effect as the distance between the electrons and holes increases.

Figure 4c provides insights into the influence of GaAs layer thickness on the diamagnetic susceptibility of the X, X^-, X^+, and XX. The figure illustrates that increasing the GaAs layer thickness results in a larger distance between the electron(s) and the hole(s), leading to higher diamagnetic susceptibility values, as expected.

An important and interesting finding from the study is presented in Fig. 5a, which depicts a combination of Figs. 3c and 4c. In Fig. 3c, the core radius has been varied from 0.3 a_0 to 2.5 a_0 while keeping the GaAs layer thickness constant at 0.8 a_0. On the other hand, in Fig. 4c, the GaAs layer thickness has been varied from 0.3 a_0 to 2.5 a_0 while fixing the core radius at 0.8 a_0. As observed in Fig. 5a, the changes in diamagnetic susceptibility are nearly identical after reaching a certain core radius or GaAs layer thickness ($\geq$0.5 a_0). This indicates that when the sum of the core radius and GaAs layer thickness is the same, it results in the same diamagnetic susceptibilities. For instance, when the core radius is 0.6 (0.8) a_0 and the GaAs layer thickness is 0.8 (0.6) a_0, the total thickness becomes 1.4 (1.4) a_0, and the diamagnetic susceptibility is nearly the same for these radius and GaAs layer thickness combinations. This finding suggests that $\langle r^2 \rangle$ must be the same for these cases.

To further verify this, biexciton probability density plots were analyzed for three different scenarios, where the core radius and GaAs layer thickness sum up to the same value, as shown in Fig. 5b. Here, the core radius (GaAs layer thickness) takes values of 0.3, 1.3, and 2.3 a_0, while the GaAs layer thickness (core radius) remains fixed at 0.8 a_0. As evident from the figure, when the core radius is 0.3 a0 (bound biexciton) and the GaAs layer thickness is 0.3 a0 (unbound biexciton), the probability densities are distinctly different from each other, while at other values (unbound biexciton) they almost completely overlap. This observation indicates that while the bound or unbound state has an impact on the diamagnetic susceptibility, the trend in binding energy is not directly reflected in the diamagnetic susceptibility, especially for X-, X+, and XX. Considering this finding could be crucial in practical applications.

Figure 6a depicts the effect of GaSb layer thickness, where the hole is localized, on the X, X^-, X^+, and XX. It can be observed that with increasing GaSb layer thickness, the total energy of all four quasi-particles undergoes a rapid decrease followed by stabilization. The increasing GaSb layer thickness causes the hole to rapidly lose energy, reducing its contribution to the total energy to negligible values compared to the electron energy. As a result, the impact of the hole on the total energy diminishes.

Figure 6b illustrates the impact of GaSb layer thickness on the binding energies. As the GaSb layer thickness increases, the attractive Coulomb potential between the electron and hole weakens, leading to a decrease in the binding energy of X. On the other hand, the binding energies of the X^-, X^+, and XX increase due to the dominance of the attractive Coulomb potential over the repulsive Coulomb potential, which diminishes the influence of the holes as the GaSb layer thickness increases. It is noteworthy that X^- and XX exhibit negative binding energies for all GaSb layer thicknesses, while X^+ initially has a negative binding energy up to 2.3 a_0 and then becomes positive.

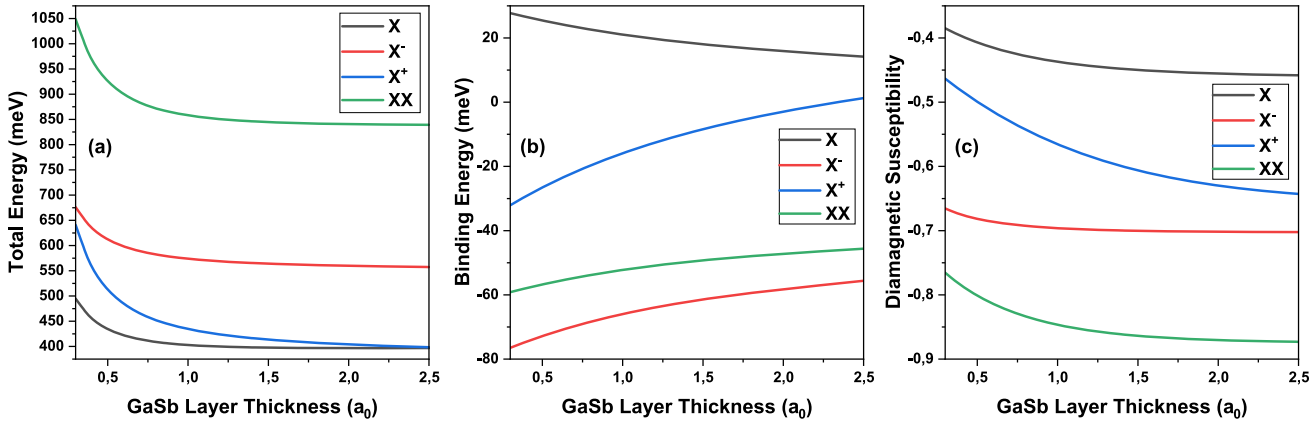

Fig. 6 Total energies (left), binding energies (middle) and diamagnetic susceptibilities (right) of the X, X^-, X^+, and XX as a function of the GaSb shell thickness

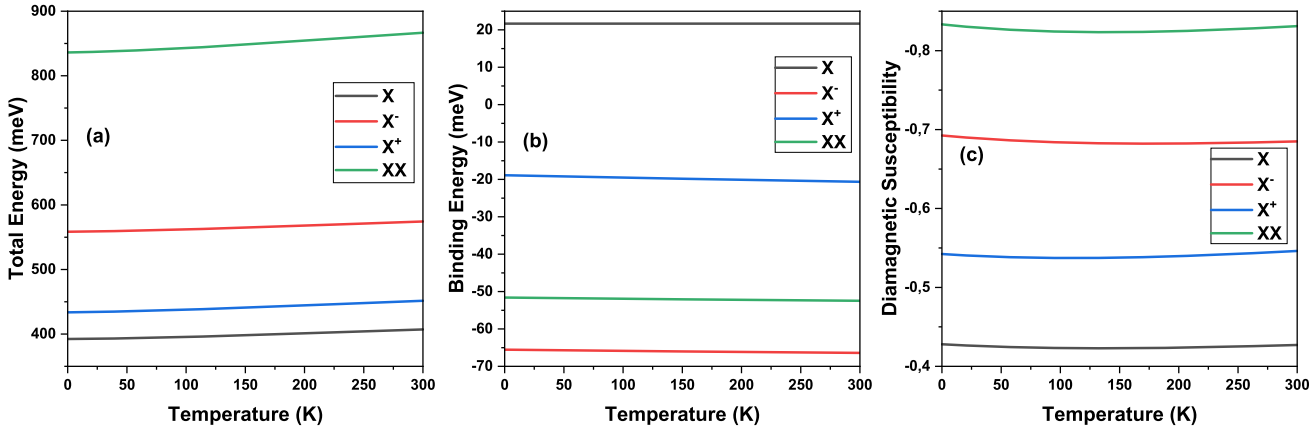

Fig. 7 Total energies (left), binding energies (middle) and diamagnetic susceptibilities (right) of the X, X^-, X^+, and XX as a function of the temperature

Figure 6c depicts the relationship between diamagnetic susceptibility and GaSb layer thickness. It is evident from the figure that the change in diamagnetic susceptibility is relatively small compared to Figures 3c and 4c. With increasing GaSb layer thickness, the holes lose energy and the repulsive Coulomb effect between them decreases, resulting in a stronger attraction toward the electrons. From this, it can be inferred that the holes are unable to move away from the electrons due to the attractive Coulomb effect, particularly in the X, X^-, and XX states. However, X^+ exhibits a slightly greater increase in diamagnetic susceptibility with increasing GaSb layer thickness, which can be attributed to the repulsive potential between the two holes within it.

In this study, the effects of temperature on total energy, binding energy, and diamagnetic susceptibility have also been investigated. While investigating the influence of temperature, the thicknesses of the InP core, GaAs, and GaSb layers have been kept at their default value of 0.8 a_0. Figure 7a is used to illustrate the variations in total energy as a function of temperature adjustments. As can be seen in the figure, there is a subtle increase in the total energies of X, X^-, X^+, and XX as the temperature increases. As shown in Fig. 8a, this temperature-induced increase directly affects the gap energies of each material, resulting in a reduction in the gap energy of each material at different rates. The amount of this reduction depends on the α and β parameters. This change in gap energies indirectly leads to a reduction in the effective masses of the electrons and holes, as elaborated in Eqs. (3) and (4), and visually depicted in Fig. 8b and c. These reductions in gap energies collectively contribute to an increase in total energies by reducing both barrier heights and effective masses.

On the other hand, as observed in Fig. 7b and c, the binding energies and diamagnetic susceptibilities of X, X^-, X^+, and XX have remained almost unchanged despite the increase in temperature. This constancy can be attributed to the fact that temperature has a similar effect on single-particle energies, regardless of whether they include the Coulomb effect or not. In addition, the increase in electron and hole energies is relatively small compared to the confinement potential, resulting in minimal changes in spatial position. As a result, the binding energies and diamagnetic susceptibility suffered negligible influence from temperature changes. In simpler terms, the strong confinement effect has effectively mitigated the influence of these small changes in electron and hole energies on the binding energy and diamagnetic susceptibility, keeping them at negligible levels.

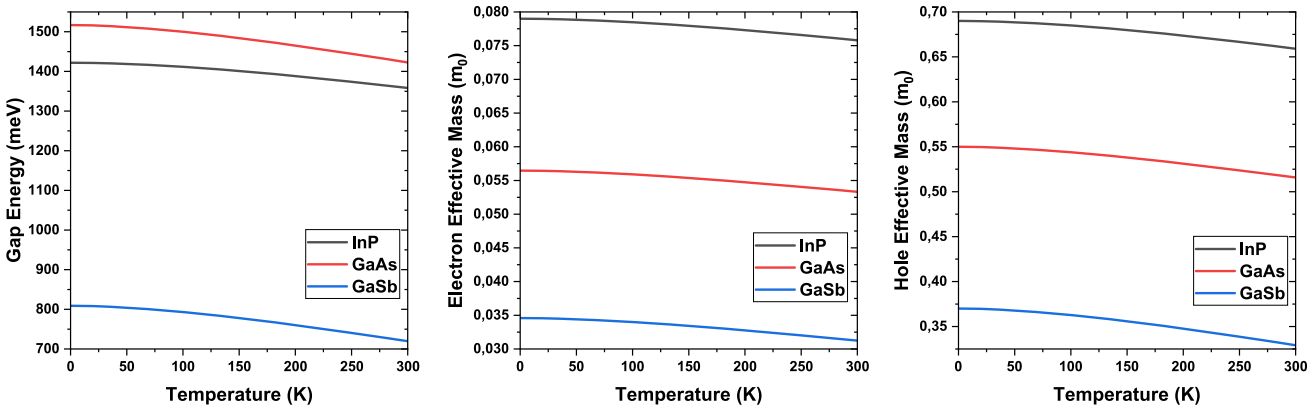

Fig. 8 Variation of gap energy (left), electron effective mass (middle) and hole effective mass (right) of InP, GaAs and GaSb with temperature

4 Conclusion

In conclusion, the total energies, binding energies, and diamagnetic susceptibilities of X, X^-, X^+, and XX in an InP/GaAs/GaSb type-II QD-HNS have been discussed with respect to the InP core radius, GaAs and GaSb layer thicknesses, and temperature. For this purpose, the Poisson–Schrödinger equation has been solved under the effective mass approximation with BenDaniel–Duke boundary conditions, taking into account the dielectric mismatch. The calculations have revealed that although diamagnetic susceptibility can offer reliable information about the stability of X, it does not fully reflect the stability of X^-, X^+, and XX. Within the quasi-type-I regime, the diamagnetic susceptibility oscillates within certain values, representing the bound state of X^-, X^+, and XX. However, in the type-II regime, drawing firm conclusions about the stability of X^-, X^+, and XX has become challenging. Particularly, when interpreting the stability of X^-, X^+, and XX, it is crucial to consider factors such as dielectric mismatch and exchange–correlation, which can have critical effects on energies despite their low influence on wave functions, in addition to the $\langle r^2 \rangle$ measurement. Another noteworthy finding regarding diamagnetic susceptibility is that, in the InP/GaAs/GaSb QD-HNS structure where holes are located in the GaSb layer, changes in the GaSb layer thickness have a significant impact on X^-, X^+, and XX binding energies, but only a minimal effect on the diamagnetic susceptibility.

Additionally, in the calculations, a critical effect of dielectric mismatch has been observed on the total energies and binding energies, specifically concerning the induced holes in the GaAs layer as the GaAs layer thickness varies. Interestingly, this effect leads to a reversal in the binding energy trend for X^- and X^+ compared to the expected behavior. Lastly, the temperature, as another variable examined in the calculations, does not have a significant effect on the total energy, binding energy, and diamagnetic susceptibility in this structure due to the strong confinement of the QD-HNS. The influence of temperature on the investigated parameters has been observed to be negligible.

Consequently, following these discussions and given the critical role of diamagnetic susceptibility in experimental research, where it provides valuable insights into the radii of excitonic formations and their bound or unbound structures, this study is expected to pave the way for more meticulous and precise interpretations of the stability of X, X^-, X^+, and XX in both experimental studies and device applications. In addition, it is expected to contribute significantly to the refinement of the calculation accuracy, especially with respect to the diamagnetic susceptibility of X^-, X^+, and XX.

Data Availability Statement This manuscript has associated data in a data repository. [Authors' comment: Data will be made available on reasonable request.]

References

1. F. Troiani, U. Hohenester, E. Molinari, Exploiting exciton-exciton interactions in semiconductor quantum dots for quantum-information processing. Phys. Rev. B **62**(4), 12263 (2000)
2. H. Kamada et al., Exciton Rabi oscillation in a single quantum dot. Phys. Rev. Lett. **87**(24), 246401 (2001)
3. H.J. Krenner et al., Recent advances in exciton-based quantum information processing in quantum dot nanostructures. New J. Phys. **7**(1), 184 (2005)
4. S.J. Boyle et al., Two-qubit conditional quantum-logic operation in a single selfassembled quantum dot". Phys. Rev. B **78**(7), 075301 (2008)
5. R. Johne, A. Fiore, Proposal for a two-qubit quantum phase gate for quantum photonic integrated circuits. Phys. Rev. A **86**(6), 063815 (2012)
6. H. Jayakumar et al., Deterministic photon pairs and coherent optical control of a single quantum dot". Phys. Rev. Lett. **110**(13), 135505 (2013)
7. V.V. Samartsev, T.G. Mitrofanova, Qubits based on the exciton degrees of freedom of a semiconductor quantum dot. J. Phys.: Conf. Series (2019). https://doi.org/10.1088/1742-6596/1283/1/012012
8. X. Wang et al., Biomass-based carbon quantum dots for polycrystalline silicon solar cells with enhanced photovoltaic performance. Energy **274**, 127354 (2023)

9. X. Mei et al., Approaching high-performance light-emitting devices upon perovskite quantum dots: advances and prospects. Nano Today **43**, 101449 (2022)
10. W. Qianqian et al., Efficient tandem quantum-dot LEDs enabled by an inorganic semiconductor-metal-dielectric interconnecting layer stack. Adv. Mater. **34**(4), 2108150 (2022)
11. P. Amini, S. Matloub, A. Rostami, Multi-wavelength solution-processed quantum dot laser. Optics Commun. **457**, 124629 (2020)
12. H. Seki, K. Miyajima, R. Shimizu, Quantum interferometric spectroscopy of a biexciton". Phys. Rev. A **106**(6), 063716 (2022)
13. X. He et al., Multicolor Biexciton Lasers Based on 2D Perovskite Single Crystalline Flakes. Adv. Optical Mater. **10**(15), 2200238 (2022)
14. S.J.W. Vonk, F.T. Rabouw, Biexciton Blinking in CdSe-Based Quantum Dots. J. Phys. Chem. Lett. **14**, 5353–5361 (2023)
15. M.A. Lampert, Mobile and immobile effective-mass-particle complexes in nonmetallic solids". Phys. Rev. Lett. **1**(12), 450 (1958)
16. J.G. Tischler et al., Fine structure of trions and excitons in single GaAs quantum dots. Phys. Rev. B **66**(8), 081310 (2002)
17. C. Galland et al., Lifetime blinking in nonblinking nanocrystal quantum dots". Nature Commun. **3**(1), 908 (2012)
18. T. Kim et al., Negative trion auger recombination in highly luminescent InP/ZnSe/ZnS quantum dots. Nano Lett. **21**(5), 2111–2116 (2021)
19. W. Rudno-Rudziński et al., Magneto-optical characterization of trions in symmetric InP-based quantum dots for quantum communication applications. Materials **14**(4), 942 (2021)
20. F. Schindler, B. Oskar Vafek, A. Bernevig, Trions in twisted bilayer graphene'. Phys. Rev. B **105**(15), 155135 (2022)
21. K.O. Pucko et al., Excitons and trions in WSSe monolayers. 2D Materials **10**(1), 015018 (2022)
22. H. Lee et al., All-optical control of high-purity trions in nanoscale waveguide. Nature Commun. **14**(1), 1891 (2023)
23. Y. Koo et al., Tunable interlayer excitons and switchable interlayer trions via dynamic near-field cavity. Light: Sci. Appl. **12**(1), 59 (2023)
24. M. Sahin, F. Koç, A model for the recombination and radiative lifetime of trions and biexcitons in spherically shaped semiconductor nanocrystals. Appl. Phys. Lett. **102**(18), 183103 (2013)
25. G.D. Scholes, G. Rumbles, Excitons in nanoscale systems. Nature Mater. **5**(9), 683–696 (2006)
26. F. Koç, A.E. Kavruk, M. Sahin, Advanced tunability of optical properties of CdS/ZnSe/ZnTe/CdSe multi-shell quantum dot by the band edge engineering. Physica E Low-Dimen. Syst. Nanostr **145**, 115479 (2023)
27. E.L. Pollock, K.J. Runge, Path-integral study of magnetic response: excitonic and biexcitonic diamagnetism in semiconductor quantum dots. J. Chem. Phys. **96**(1), 674–680 (1992)
28. M. Stern et al., Mott transition of excitons in coupled quantum wells". Phys Rev. Lett. **100**(25), 256402 (2008)
29. Z. Avazzadeh et al., Diamagnetic susceptibility of an off-center hydrogenic donor in pyramid-like and cone-like quantum dots. The European Physical Journal Plus **131**, 1–8 (2016)
30. G. Vignesh, P. Nithiananthi, Effect of confinement potential on exciton diamagnetism in the perspective of constituent carriers in a Quantum Well. Journal of Physics and Chemistry of Solids **114**, 187–194 (2018)
31. F. Koc, M. Sahin, Electronic and optical properties of single excitons and biexcitons in type-II quantum dot nanocrystals. J Appl. Phys. **115**(19), 193701 (2014)
32. A. Aktürk et al., A detailed investigation of electronic and optical properties of the exciton, the biexciton and charged excitons in a multi-shell quantum dot nanocrystal. J. Phys. D: Appl. Phys. **47**(28), 285301 (2014)
33. D.J. BenDaniel, C.B. Duke, Space-charge effects on electron tunneling. Phys. Rev. **152**(2), 683 (1966)
34. M. Sahin et al., Reordering orbitals of semiconductor multi-shell quantum dot-quantum well heteronanocrystals. J. Appl. Phys. **111**(2), 023713 (2012)
35. A. Sadao, *Properties of group-iv, iii–v and ii–vi semiconductors* (Wiley, Hoboken, 2005)
36. M. Sahin et al., Self-consistent computation of electronic and optical properties of a single exciton in a spherical quantum dot via matrix diagonalization method". J. Appl. Phys. **106**(4), 043704 (2009)
37. S. Rajashabala, K. Navaneethakrishnan, Effects of dielectric screening and position dependent effective mass on donor binding energies and on diamagnetic susceptibility in a quantum well. Superlatt. Microstr. **43**(3), 247–261 (2008)
38. J. Zipfel et al., Spatial extent of the excited exciton states in WS 2 monolayers from diamagnetic shifts. Phys. Rev. B **98**(7), 1075438 (2018)
39. A. Brumberg et al., Determination of the in-plane exciton radius in 2D CdSe nanoplatelets via magneto-optical spectroscopy. ACS Nano **13**(8), 8589–8596 (2019)
40. J.P. Philbin, E. Rabani, Auger recombination lifetime scaling for type I and quasi-type II core/shell quantum dots. J. Phys. Chem. Lett. **11**(13), 5132–5138 (2020)
41. J.P. Perdew, A. Zunger, Self-interaction correction to density-functional approximations for many-electron systems. Phys. Rev. B **23**(10), 5048 (1981)
42. T. Tsuchiya, Biexcitons and charged excitons in quantum dots: a quantum Monte Carlo study". Physica E: Low-Dimens. Syst. Nanostr. **7**(3–4), 470–474 (2000)
43. I. Vurgaftman, L. JáR Meyer, R. Ram-Mohan, Band parameters for III-V compound semiconductors and their alloys'. J Appl. Phys. **89**(11), 5815–5875 (2001)
44. T.A.S. Pereira et al., On the interplay between quantum confinement and dielectric mismatch in high-k based quantum wells. J. Appl. Phys. **108**(5), 054311 (2010)